JOURNAL OF AIRCRAFT
Vol. 47, No. 1, January–February 2010

Advanced Experimental and Numerical Validation and Analysis of Propeller Slipstream Flows

Eric W. M. Roosenboom*
DLR, German Aerospace Research Center, 37073 Göttingen, Germany
Arne Stürmer†
DLR, German Aerospace Research Center, 38108 Braunschweig, Germany
and
Andreas Schröder‡
DLR, German Aerospace Research Center, 37073 Göttingen, Germany

DOI: 10.2514/1.45961

A comparison of velocity(-derived) quantities is made in the slipstream of a turboprop-equipped transport aircraft between phase-locked experimental Particle Image Velocimetry data and unsteady Reynolds averaged Navier–Stokes calculations. Velocity results indicate a high level of agreement between the numerical and experimental results. In addition to velocity vector data, other derived quantities, such as vorticity, allow a verification and validation of the modeling in Computational Fluid Dynamics. Although a good agreement is achieved, future needs for the comparison and validation of computational (Computational Fluid Dynamics) and experimental (Particle Image Velocimetry) data are highlighted.

Nomenclature

C_D = drag coefficient
C_L = lift coefficient
C_T = thrust coefficient
C_Y = lateral force coefficient
D = propeller diameter, m
dA = integration area, m
$f_\#$ = focal number
J = advance ratio
x = distance in flow direction, m
Γ = circulation, $m^2 \cdot s^{-1}$
ψ = time history, deg
ω = (out-of-plane) vorticity, s^{-1}

I. Introduction

PROPELLER flow is highly complex and its aeronautical research has long been overshadowed by turbofan applications. Because of high oil prices there is a revived interest in propeller technology, which requires enhanced predicting capabilities for such flows. Advances have been made over the years for numerical calculations. Direct numerical simulations can solve a fully turbulent flow without approximations, albeit at low Reynolds numbers. Such calculations are not yet achievable for complex turbulent unsteady rotational flows, such as the determination of the flow around an aircraft equipped with propellers, mainly because the method is computationally exhaustive. Although large eddy simulations (LES) are less computational extensive, they still require significant computational effort [1]. Reynolds averaged Navier–Stokes (RANS), and its unsteady counterpart uRANS, have developed into widely applicable methods that can be applied to a broad variety of flows in a standardized fashion [2,3]. In addition, these recent developments in numerical calculations have sparked an interest in the need for validation techniques [4,5]. Any (aeronautical) computational code that simulates complex shear layer interactions, turbulence, vortical regiments, and energy transfer and dissipation in boundary layers has to be verified and validated with appropriate measurements and especially for complex flow phenomena occurring at propeller–wing interactions and their influence on aircraft stability.

Particle Image Velocimetry (PIV) is in particular suitable, perhaps exclusively, for the comparison of (instantaneous) velocity vector fields [6]. In addition, well-prepared PIV measurements provide an extensive database with velocity-derived quantities (vorticity, instantaneous fluctuations, velocity fluctuations, turbulence kinetic energy, and Reynolds stresses) that can be used to compare and characterize the capabilities of computational methods with respect to turbulence properties as well as for computational aeroacoustic simulations [6]. From a point of view regarding the validation of propeller flow, there is very little literature available; see, for example, [7] in which a satisfactory comparison of Euler calculations and PIV data is given. Cho and Cho [8] reported on the 3-D steady vortex lattice method for the propeller and a 3-D unsteady panel method for the wing for unsteady propeller–wing interactions but indicated that, apart from the need for increased accuracy for higher revolutions (and blade numbers), experimental data at higher frequencies should also be made available for comparisons between computational and experimental propeller data.

Apart from validation and verification, advanced research on propeller flow influence is needed to estimate the effects of airframe engine installation and to establish the propeller slipstream effects on the wing. A mutual approach by considering both vorticity and turbulence properties based on experimental and computational data allows one to address the validation and maturity of Computational Fluid Dynamics (CFD) codes as well as the overall effect those properties have on the aircraft design. We intend to provide a database of experimental and computational data that can be used for the comparison and validation of several velocity-derived quantities. These data are a result of the inherent modeling of computational methods. This paper describes the ongoing work of validating and expanding existing CFD tools for the analysis of propeller flow with experimental velocity (PIV) data.

Presented as Paper 3626 at the 27th AIAA Applied Aerodynamics Conference, San Antonio, TX, 22–25 June 2009; received 12 June 2009; revision received 19 August 2009; accepted for publication 22 August 2009.

*Research Scientist, Experimental Methods, Institute of Aerodynamics and Flow Technology, Bunsenstraße 10; eric.roosenboom@dlr.de. Senior Member AIAA.

†Research Scientist, Transport Aircraft, Institute of Aerodynamics and Flow Technology, Lilienthalplatz 7.

‡Research Scientist, Experimental Methods, Institute of Aerodynamics and Flow Technology, Bunsenstraße 10. Member AIAA.

II. Advanced Propeller Model

The propeller aircraft models for both the experiments and computations are based on a design for an advanced military transport aircraft. The transport aircraft itself is designed for a multitude of tactical missions, such as starting from short runways, cargo dropping, and steep descents and takeoffs. A high installed power is required to fulfill all requirements. Because of the high installed power, a standard asymmetric propeller configuration (i.e., all propellers rotating in the same direction) is unfavorable [3]. An unconventional design is used in which the propellers rotate in opposite directions, mainly as an optimization of multiple conflicting technical considerations (i.e., the best performance in cruise and high-lift conditions) at the high installed engine power [3]. The rotating direction is referred to as "down between engines" to refrain from a misinterpretation of the terms "counter-rotating" and "contra-rotating." The opposite direction of rotation directions necessitates the use of two sets of propellers for the wind-tunnel model (clockwise and counterclockwise).

A. Wind-Tunnel Model

The wind-tunnel model is mounted to the ceiling of the wind tunnel. Pressurized air is used to drive both propellers and supplied through connections in the wind-tunnel ceiling. The inlet air is heated to prevent icing on parts of the wing and propeller. The propellers are equipped with rotary shaft balances (RSB) that enable the measurement of forces and moments of the propellers. An initial signal (1 per revolution) activates multiple subsequent signals that are used to monitor the revolutions of the RSB using a specialized software system. This initial signal can be used as a transistor–transistor-logic (TTL) signal to trigger the PIV equipment (laser pulses and camera acquisition). The propeller blades are constructed of carbon fiber and their blade pitch angle is set individually. The propeller scale is 1:17 with respect to the full-scale model and it implies that, to match the advance ratio and power settings in flight, the propeller revolutions should be significantly higher than they would occur in flight. Moreover, the maximum available power for such a highly loaded wind-tunnel model is in the order of about 50 kW per propeller.

B. Computational Fluid Dynamics Model

For the CFD simulation, the geometry of the aircraft as tested in the wind tunnel is fully replicated in the CAD model. As in the experimental test campaign, it consists of the fuselage, sponson, and wing, including the flap track fairings and the high-lift system in the appropriate setting, as well as the nacelles and the propellers. The simulations do not include a modeling of the wind tunnel itself and thus no peniche is used. The pitch angle of the blades of both propellers is set to the corresponding angles used for the reference conditions in the test. Thanks to the counter-rotating propellers with a "down-between-engines" sense of rotation on each wing the simulations were performed for a half-model, using a symmetry plane along the centerline of the aircraft.

III. Methodologies

The comparison is based on calculations performed using unsteady Reynolds averaged Navier–Stokes calculations and phase-locked experimental PIV data. Instantaneous velocity data sets are measured with PIV. Using planar PIV, one typically obtains thousands of velocity vectors per particle double image and field of view. A standard approach after evaluating the instantaneous PIV velocity vector fields is to use an averaging approach over the obtained instantaneous vector fields to observe average phenomena in the flowfield. Similar to the uRANS technique, such an approach is based on the Reynolds decomposition technique, in which the velocity is regarded as the sum of an average velocity and a fluctuation term. From the instantaneous velocity fields, the root mean square (standard deviation) of the data set can be calculated. The Reynolds decomposition based on flow statistics allows the determination of the turbulent shear (one of the terms of the Reynolds stress tensor) in planar PIV. These properties exhibit the origin of uRANS calculations and are an indication of the accuracy of PIV measurements. Verifying and comparing these turbulent properties is required for a detailed computational and experimental insight into flow structures in a propeller slipstream. Sections III.A and III.B indicate the specific details of the numerical calculations and the experiment settings. The Reynolds number in both the experiments and numerical analysis was roughly 1.25×10^6. Other parameters such as freestream conditions are all obtained from the wind-tunnel data, so that in the numerical evaluation the experimental conditions are matched.

A. Details Particle Image Velocimetry Experiment

1. *Experimental Setup*

Particle Image Velocimetry is a nonintrusive whole-field velocity measurement technique [9]. The capabilities of PIV range from low- to high-speed applications. Nowadays, PIV is readily applicable in industrial facilities [10]. The setup used in the experiments is described in more detail in [11], and is summarized here briefly. Results of the application of pressure sensitive paint (PSP) are reported elsewhere [12]. The laser light sheet optics (Fig. 1a) and four high-resolution charge-coupled device cameras (in a two-component arrangement) are coupled by a traversing system. In addition, the camera system is connected to the wind-tunnel turntable; see Fig. 1b. It has the advantage that the field of view corotates with the wind tunnel for various angles of attack. This facilitates fast progress with only a minimal need for calibrations. Subsequent measurements in several planes are easily performed. The PIV measurements are obtained in a phase-locked sense, in which a TTL signal is used to trigger the acquisition of PIV images [13]. At each phase orientation, 200 image pairs are acquired. The focal length of the lenses was 100 mm and $f_\#$ was at 2.8. Two double-cavity Big Sky CFR 200 Nd:YAG lasers with an output of 400 mJ per pulse were used to illuminate the seeding particles. The pulse duration of one pulse is approximately 9 ns, yielding a negligible angular displacement of 8×10^{-4} deg based on the (maximum) rotational speed of the propeller. Diethylhexyl sebacate droplets with an average diameter of 1 μm have been used as seeding material and were generated by two Laskin-type nozzle-equipped aerosol generators [14]. Homogenous seeding was ensured in the test section. Parts of the wind-tunnel model have been painted black with a special mixture of black acrylic and Rhodamine 6G, which reduces laser light reflections.

2. *Pre- and Postprocessing*

The cross correlation of the recorded particle images is not as straightforward as it seems and mostly requires pre- and post-processing. Standard preprocessing procedures include image enhancement via low (smoothing, noise reduction) and high (increase detail) pass filtering techniques and minimum image subtraction such that the signal-to-noise ratio of the images is optimal before it is analyzed with the cross-correlation software. The software used for the analysis is PIVview 2.3. The software package uses multigrid

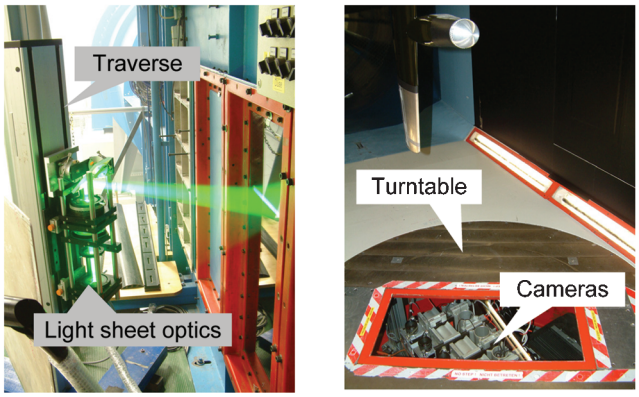

a) Light optics on traversing system **b) Overview of wind-tunnel model, turntable, and cameras**

Fig. 1 Overview of experimental setup.

interrogation with image deformation. Outlier detection [15] is used to remove spurious vectors (about 0.5% of the vectors were identified as outliers).

B. Details of Unsteady Reynolds Averaged Navier–Stokes Simulation Approach

The uRANS simulations are performed using the DLR TAU code [16], an unstructured finite volume vertex-based CFD solver developed at the DLR, German Aerospace Research Center's Institute of Aerodynamics and Flow Technology. For the simulation described here, spatial discretization of the convective fluxes is done using a second-order central differencing scheme with matrix dissipation, whereas the viscous fluxes are discretized with central differences. Fully turbulent flow is prescribed, that is, no transition phenomena are accounted for, and the one-equation turbulence model of Spalart–Allmaras as modified by Edwards and Chandra [17,18] is employed. The computation of propeller flows presents some unique requirements for the CFD method. The solver must be capable of handling multiple rigid bodies in relative motion, because the propeller needs to rotate relative to the stationary nacelle, and it must be possible to compute a time-accurate unsteady solution. The well-established dual-time approach is used in the DLR TAU code to compute unsteady flows [19]. For each discrete physical time step, a solution is obtained through a time-stepping procedure in a pseudo-time, making use of the same convergence acceleration techniques used for steady-state computations, namely, a three-stage Runge–Kutta scheme, local time stepping, multigrid, and residual smoothing. To simulate the relative motion of the propellers, this simulation draws on the TAU code's Chimera capability as well as the implemented motion libraries [20,21]. TAU can be efficiently used on scalar as well as on vector computers and on massively parallel machines using message-passing-interface-based parallelization. TAU has been widely applied to and validated for the simulation of propeller flows in recent years, leading to the development of best practice guidelines for its use for these types of computations [2].

1. *Grid Generation*

For the simulations discussed here, a three-block Chimera mesh is used, which was generated with the CentaurSoft Centaur grid generation software.[§] This tool has been employed extensively at DLR, German Aerospace Research Center for various unstructured grid-based CFD applications. The Chimera grid approach as implemented in TAU requires taking special care during the creation of the CAD geometry, as it is necessary to prescribe two cylindrical holes in the aircraft grid block at the position of the propellers. In addition, an adequate overlap of the separately generated aircraft and propeller grids needs to be assured through the appropriate positioning of the geometric boundaries that make up the Chimera interfaces.

The first of the three grid blocks is generated around the aircraft consisting of the fuselage, sponson, wing, flap track fairings, high-lift systems, and the nacelles. A so-called hybrid mesh is created, which uses 25 layers of semistructured prismatic elements in the vicinity of the aircraft surfaces for a good boundary-layer resolution. The spacing for the first cell is set to ensure that a y^+ value of around 1 is achieved in the CFD simulation. The remainder of the flowfield is meshed with tetrahedral elements, for which the Centaur functionality of localized mesh refinement through the use of so-called sources is used to create very fine meshes in the regions of the propeller slipstream to enable an improved resolution of the propeller–wing interactions. The aircraft mesh block has a total size of 23,782,250 nodes. For the generation of the propeller meshes, the periodic nature of the geometry is exploited. Only a 90 deg segment, that is, one blade passage, was meshed and the complete propeller mesh was then obtained through subsequent copying, rotating, and merging. This procedure is an important ingredient in ensuring that periodic aerodynamic results are more easily achieved, as each blade passage features an identical spatial discretization. As both propellers have identical blade pitch settings, the second propeller mesh is obtained through a simple mirroring of the first. To keep grid sizes at a manageable level for this first large-scale simulation of unsteady installed propeller flows at high-lift conditions, the propeller surfaces are treated as inviscid walls here, leading to a fully tetrahedral mesh with 6,327,540 nodes for each propeller.

The three-block Chimera mesh is then created through the merging of the appropriately positioned grid blocks, resulting in a total mesh size of 36,437,330 nodes. Figure 2 shows a section of the grid along the centerline of the outboard propeller, which highlights the Chimera grid approach (the blue grid of the propeller block and the black grid of the aircraft grid) as well as the introduced refinement in the region aft of the propeller for proper slipstream resolution.

2. *Unsteady Reynolds Averaged Navier–Stokes Simulation*

The uRANS simulations were run on 96 CPUs and were initiated from scratch, that is, with the flowfield initialized to far-field conditions. The flow conditions set for the computation correspond to one test point covered in the wind-tunnel campaign and are typical low-speed, high-angle-of-attack approach conditions with a corresponding propeller thrust setting. As in the test, both propellers were set to rotate at identical rotational speeds. As mentioned earlier, a fully turbulent simulation was performed employing the one-equation Spalart–Allmaras turbulence model. To speed up the computation, a sequential reduction of the physical time step size along with a stepwise refinement of the number of inner iterations in the dual time method during the course of the simulation was done. This approach allows for a more rapid propagation of the initial disturbances at the beginning of the simulation and a quicker achievement of the periodic state of the flowfield. To obtain data with high accuracy for the analysis, the final settings of the dual time method for the last few propeller rotations were a physical time step size corresponding to a 1 deg propeller using 200 inner iterations at each individual time step.

Overall, 55 propeller rotations were computed. Figure 3 shows the time history of the aircraft force coefficients during the course of the simulation. It can be seen that, in the mean, each of the force coefficients has achieved a constant value during about the five final prop rotations. Unsteady interactions between the propeller and the airframe are the cause for the periodic oscillations that are visible in the figure.

IV. Comparison of Results

In the experimental test campaign PIV measurements were obtained in a total of five flow-aligned planes for the outboard propeller, as shown in Fig. 4. They are numbered sequentially from the outboard plane (E1) through the inboard plane (E5). The PIV

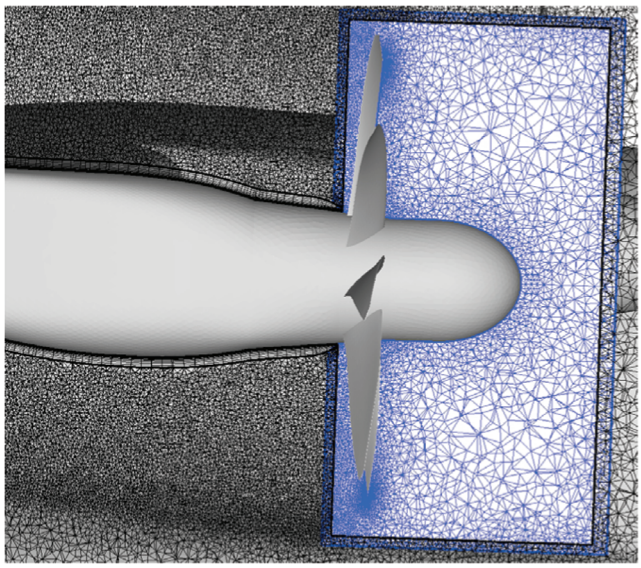

Fig. 2 Slice through the CFD mesh.

[§]Data about CentaurSoft available online at http://www.centaursoft.com [retrieved 12 Dec. 2008].

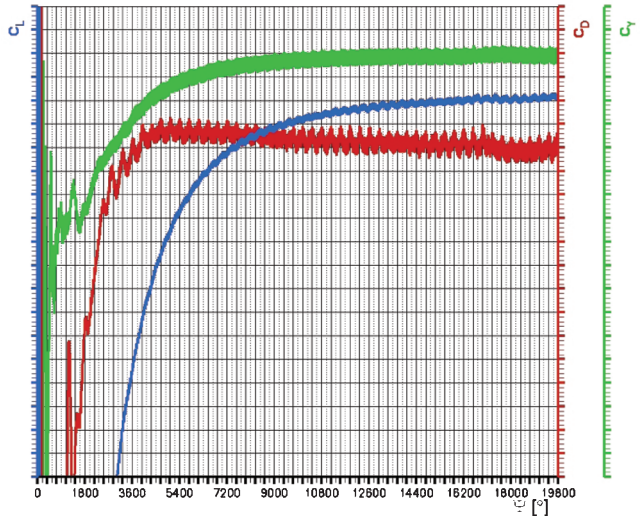

Fig. 3 Time history of aircraft force coefficient development.

setup was optimized for optical access to measure the plane along the outboard engines centerline, E3. The planes E1 and E5 are located close to the respective propeller edge of the slipstream. A comparison between the experimental and numerical data is presented in terms of absolute velocity and vorticity contours. For the latter, the absolute magnitude of the out-of-plane vorticity component is shown, as planar PIV only provides a 2-D velocity field [9]. The results of the computational and experimental analysis are presented for an identical advance ratio, J, and thrust setting, C_T.

A. Propeller Slipstream Development

The interaction of the propeller slipstream with wing and high-lift systems at the high-angle-of-attack, low-speed flight conditions studied here lead to a very complex flow topology. To support the comparison between the PIV and the CFD results in this section, Fig. 5 shows a 3-D view of the wing suction side aft of the outboard propeller to help clarify the complex flow phenomena. Here the vorticity contours shown are based on the full 3-D velocity field and the upper slipstream boundary is blanked so as to obtain a clear view of the vortical structures near the wing surface. In addition to the tip vortex, the propeller slipstream for this fully installed configuration features a very pronounced nacelle vortex, which, due to the direction of rotation of the propeller, is formed at the outboard junction of the nacelle with the wing leading edge. This vortex is propagated over the wing suction side just outboard of the engine centerline. Equally important are the vortical structures due to the blade wakes, which are marked in Fig. 5. Again, due to the direction of rotation of the propeller, a diagonal vortical structure is formed on the wing suction

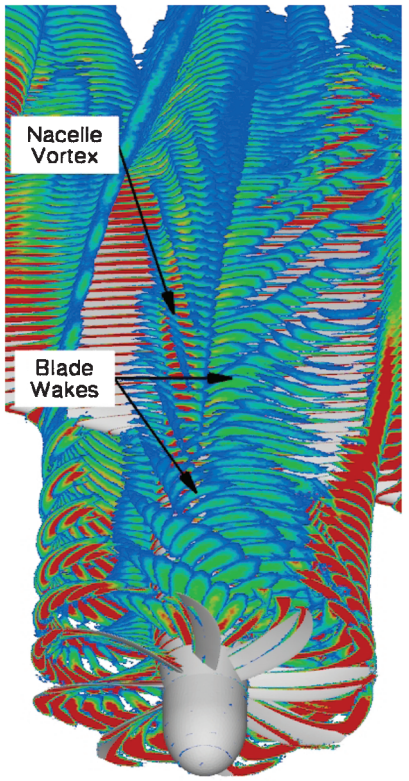

Fig. 5 Suction side propeller slipstream flow topology development during the interaction with the wing (CFD).

side that moves in the flow direction inboard of the engine centerline. On the pressure side of the wing similar structures exist, but they are found outboard of the engine centerline.

Figure 6 compares PIV and CFD results for the engine centerline plane E3, with absolute velocity contours shown in Fig. 6a and the out-of-plane vorticity in Fig. 6b. Qualitatively, the CFD-predicted propwash development is seen to be in good agreement with the experimental data, with similar structures found at the slipstream boundary. It is evident though, that the numerical results show slightly higher velocity magnitudes than those found through PIV. Although it appears that a qualitative agreement between the experimental and numerical data is also found in terms of (out-of-plane) vorticity, Fig. 6b, it will be shown later that there is a quantitative mismatch between the experimental and numerical results in terms of circulation. The locations of the tip vortices as well as their development during the propagation of the propeller slipstream over the wing are predicted quite well by CFD. Overall vorticity contours in the numerical results are a bit more blurred than seen in the PIV results (partly attributable to the postprocessing

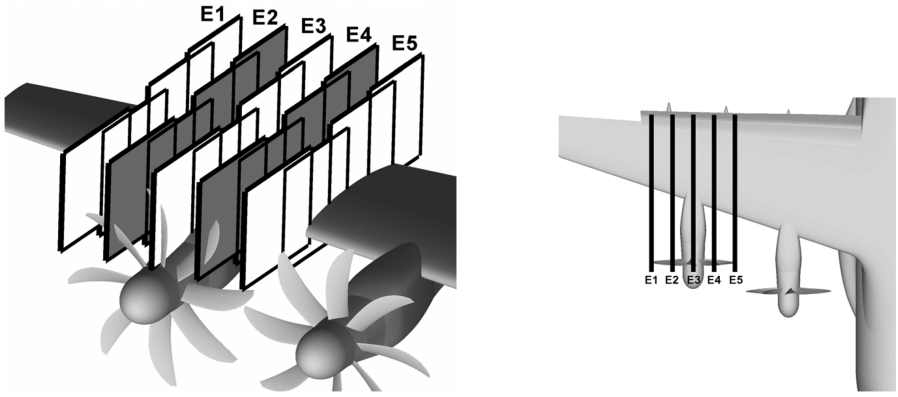

a) 3-D view of the initial (before interpolation) PIV camera field of views **b) Top view**

Fig. 4 Overview of spanwise positions for comparison.

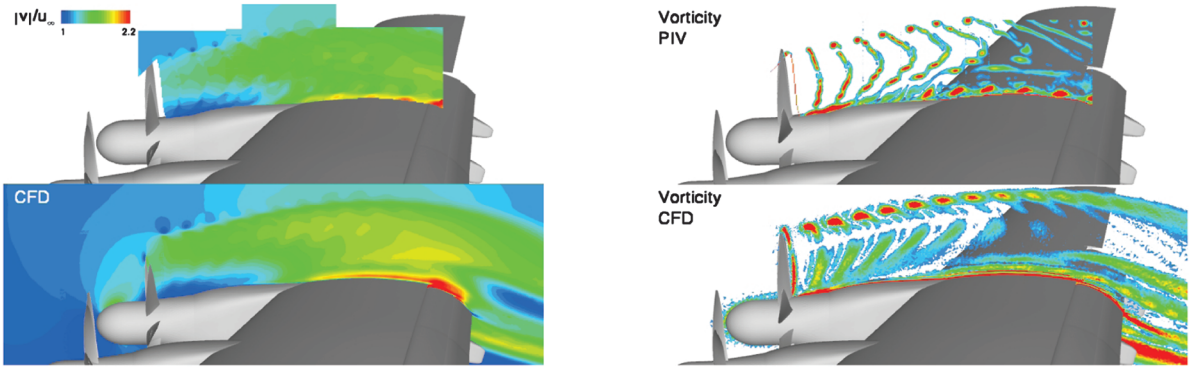

a) Outboard engine centerline absolute velocity contours **b) Outboard engine centerline vorticity contours**

Fig. 6 Comparison in propeller symmetry plane (E3).

of the CFD data on the unstructured mesh and partly caused by numerical dissipation effects). This holds in particular for the blade wakes, which are quite clearly defined in the experimental results and much less so in the TAU uRANS data. In addition to this difference, another discrepancy is found near the wing suction side surface.

The PIV results show the presence of concentrated circular regions of higher vorticity just above the airfoil, pointing to the presence of vortices. These structures are not as clearly defined in the CFD, but their presence is nonetheless visible primarily as they emerge and separate from the main wing boundary layer toward the trailing edge of the wing. This can be seen in the clearly distinguished circular regions of higher vorticity above (and below) the main wing shear layers as the flow is deflected by the flaps in the extreme right of Fig. 6b. As discussed for Fig. 5, these structures are caused by the blade wakes. The less pronounced vorticity in these vortices is thus directly related to the previously observed reduced strength of the blade wakes in the TAU uRANS simulation. The presence of the nacelle vortex can be seen at least somewhat toward the trailing edge of the main wing in both the PIV and CFD results, wherein slightly increased levels of vorticity are seen above the blade wake structures and the boundary layer. As this vortex is primarily aligned with the flow direction, it does not lead to a significant increase in the out-of-plane vorticity used here.

The comparison of vorticity in the remaining in- and outboard planes (Fig. 7) indicate differences between the experimental and numerical results. As the experimental setup was prepared for the investigation of the (outboard) propeller symmetry plane, the necessary compromise in terms of optical access becomes evident for the outermost planes shown in Figs. 7a and 7d. While traversing in spanwise directions, it follows that due to the dihedral angle of the wing the field of view is not optimal in some of the other planes. Therefore, in the PIV result in Fig. 7a, part of the velocity information "above" the nacelle is not available.

Plane E1 shown in Fig. 7a lies right on the outer boundary of the propeller slipstream. Thus, the only noticeable slipstream effect

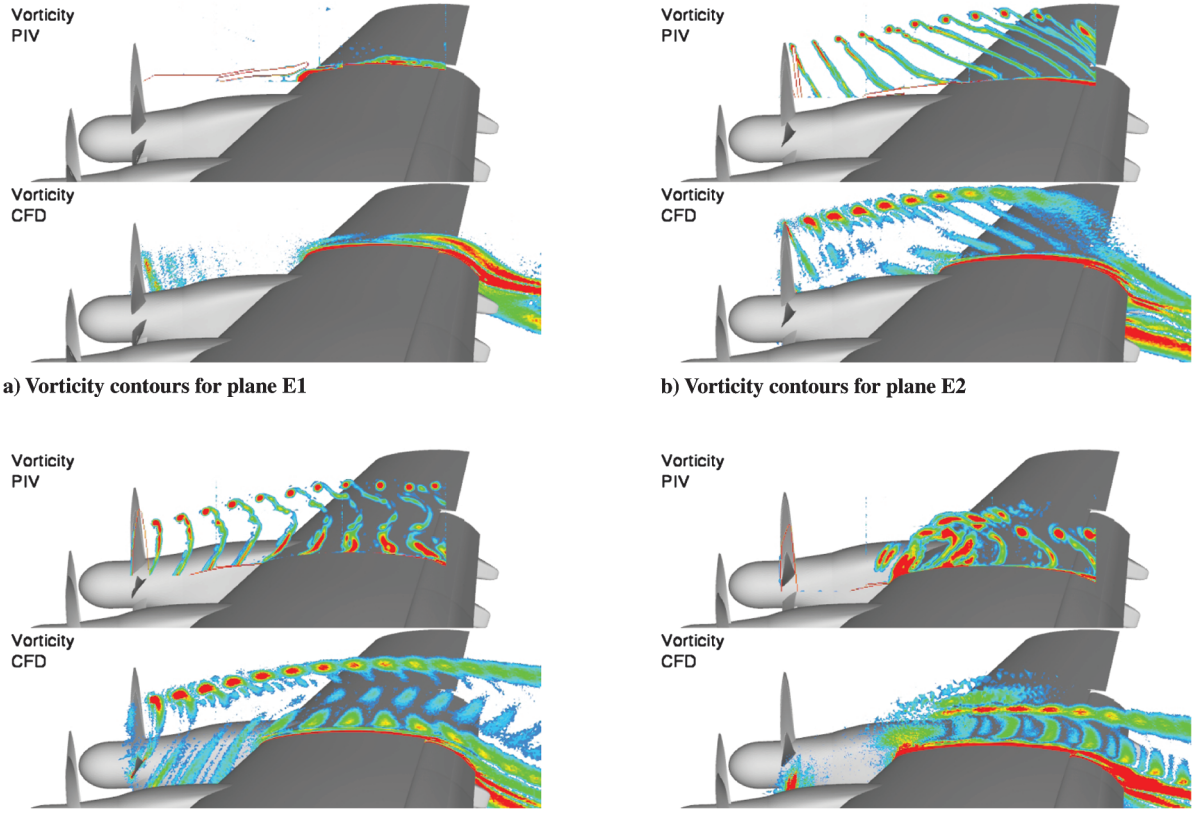

a) Vorticity contours for plane E1 **b) Vorticity contours for plane E2**

c) Vorticity contours for plane E4 **d) Vorticity contours for plane E5**

Fig. 7 Comparison of vorticity contours at several stations.

visible is the nacelle vortex. This shows up again as a region of increased vorticity toward the trailing edge of the wing, which seems to be more pronounced in the TAU results. For plane E2 in Fig. 7b, the observations made for the engine centerline plane can be essentially repeated. Inboard of the engine centerline, plane E4 (Fig. 7c) shows an increase in the vorticity levels of the blade-wake-induced vortices near the wing suction side both in the experimental and numerical results. Once again, although globally agreement is good, the numerical results do show more dissipated vortical structures as well as generally weaker blade wakes than seen in the experimental data. Finally, the innermost plane, E5 in Fig. 7d, reveals some more pronounced differences between the two data sets. In the CFD simulation, the propeller rotation was prescribed to be perfectly synchronized with the blade passage perfectly in phase. Although the propeller operation in terms of rotational speed was monitored during the experiments, small fluctuations are inevitable. Thus, the propellers are not exactly synchronized during the wind-tunnel test, which is thought to be the cause for the observable differences in vortical structures near the leading edge of the wing in Fig. 7d.

B. Determination of Circulation

It is observed in the vorticity plots of Fig. 6b that there is a difference in the vorticity distributions that is partially attributed to numerical dissipation effects. To further assess the observed difference between the experimental and numerical data, the circulation in the tip regions is calculated. The contraction of the slipstream and resulting changes in (induced) velocity are required for various theoretical propeller models [22], and the radial distribution of the circulation is a direct measure of the distribution of the lift of a propeller blade (i.e., thrust). In the current numerical and experimental results, large interactions are observed in the boundary layer. The large complexity of available data diffuses the observations between experimental noise sources and numerical dissipation effects in this area. To quantify and asses this extent, integral values can be compared on areas that are not obscured by either experimental noise or numerical dissipation. In both the experiment and numerics, the tip vortices are well resolved; these are therefore suitable for a comparison of circulation strengths. It is recognized that with such an analysis the single distribution to thrust of one propeller blade cannot be resolved. It provides, however, a basis for comparison and reference for future improvements. A threshold is applied to distinguish the noise in the experimental results. The threshold is chosen to be 2% of the maximum value of the vorticity (in either PIV or CFD) and is applied to both numerical and experimental data. This resulting positive vorticity is then subsequently used to determine the circulation using the relation (before the area integration, it has been ensured that the CFD data have nearly the same grid points as the PIV data via linear interpolation):

$$\Gamma = \oint \omega \cdot \mathrm{d}A \tag{1}$$

Results for the calculation in the symmetry plane are listed in Table 1 (all values are normalized by the first vortex). Particularly interesting is the trend in the circulation values that show that the circulation is reduced for the CFD results, whereas for the PIV results the circulation distribution rises at the first two vortices and remains fairly constant. This supports the conclusion that numerical dissipation negatively affects the capability to fully resolve the vorticity in the CFD calculations.

Table 1 Values of positive circulation strength of tip vortices (normalized by first vortex)

	1	2	3	4	5	6	7
PIV	1.00	1.15	1.28	1.32	1.31	1.19	1.34
CFD	1.00	0.96	0.88	0.78	0.72	0.67	0.66

C. Cause of Deviations

Considering the complexity of the model aircraft in a high-lift configuration, which includes everything but the tailplane, as well as the highly intricate flow physics of propeller–airframe interactions, the agreement seen between the numerical and experimental results is quite remarkable. Generally it is found that the developments of the propeller slipstream during its propagation over the wing as well as the associated vortical structures are well-predicted in the uRANS results. As mentioned, some differences are of course observed, the causes of which are discussed in this section.

A source of uncertainty on the PIV side could be the use of the four cameras in planar fashion, which requires special attention for alignment and calibration. Although great care for detail was ensured (on average, less than 0.5% vectors were outliers), some outliers are inevitable and manifest themselves in overlapping regions. The edge effects result from small projection errors made systematically when using two-component, 2-D PIV with one single camera per field of view. In the regions with overlapping grids it is possible to reduce outliers and artifacts by using a linear interpolation. Therefore, the experimental results presented are interpolated on one rectangular grid.

For the uRANS simulation, a number of parameters are important contributors to the accuracy of the numerical results. For tip vortex resolution, the TAU results show good agreement with the trends seen in PIV in terms of location, general magnitude, and temporal development. The primary issue on the CFD side can be found in the impact of numerical dissipation, both driven by the nature of the CFD algorithms as well as the impact of the unstructured mesh. Although the use of matrix dissipation as well as the refined mesh in the propeller slipstream region has been quite successful in capturing and sustaining these flow features in their interaction with the wing, a smearing and somewhat premature dissipation of the vortices is evident in comparison with the PIV data, as discussed in the previous section. The turbulence model used in these simulations is the one-equation model by Spalart–Allmaras as modified by Edwards. It is known that this particular model, as well as one-equation models in general, tends to overpredict the magnitude of eddy viscosity in vortex cores, contributing to the premature diffusion of these flow structures. This is due to the formulation of the production term in the model, which is based on the flow vorticity. In vortex cores, however, this leads to an excess level of eddy viscosity being computed, neglecting the suppression effect the pure rotational nature of the flow has on turbulence [23,24].

As mentioned, it is generally found that slightly higher velocities are seen in the propeller slipstream numerical data than through PIV. Seen qualitatively in Fig. 6a, Fig. 8a plots the absolute velocity profiles in the plane along the engine centerline at an axial position of $x/D = 1.0$ and 1.5 aft of the plane of propeller rotation for a quantitative comparison. Comparing, for example, the solid black line, representing the CFD data at $x/D = 1.0$, with the solid green line, plotting the corresponding PIV data, the increased magnitude throughout the entire slipstream region in the numerical results is visible. The difference in peak magnitude is about 6%. The general shape of the profile is quite comparable though, substantiating the earlier claim of very good agreement globally in general slipstream characteristics and development between the TAU results and the experimental data. This is also evident when comparing the respective profile development in the axial direction from the position at $x/D = 1.0$ and 1.5 for CFD (solid versus dash-dotted black line) and PIV (solid and dash-dotted green line).

The cause of the higher velocities in the CFD results can be traced to the inviscid modeling of the blades, which was done to keep the mesh size manageable for this first large-scale application. Because of this simplified modeling, the velocity deficit in the blade wakes is naturally not properly accounted for. Figure 8b, plotting the propeller slipstream development in the wake of the isolated propeller at axial flow using an inviscid versus a viscous modeling of the blades at the top and bottom, respectively, clearly shows that the neglect of the blade wakes leads to an overall slight increase in propwash velocities in the former case. Also, although blade wakes are seen to be sustained well past the main wing trailing edge in the experimental

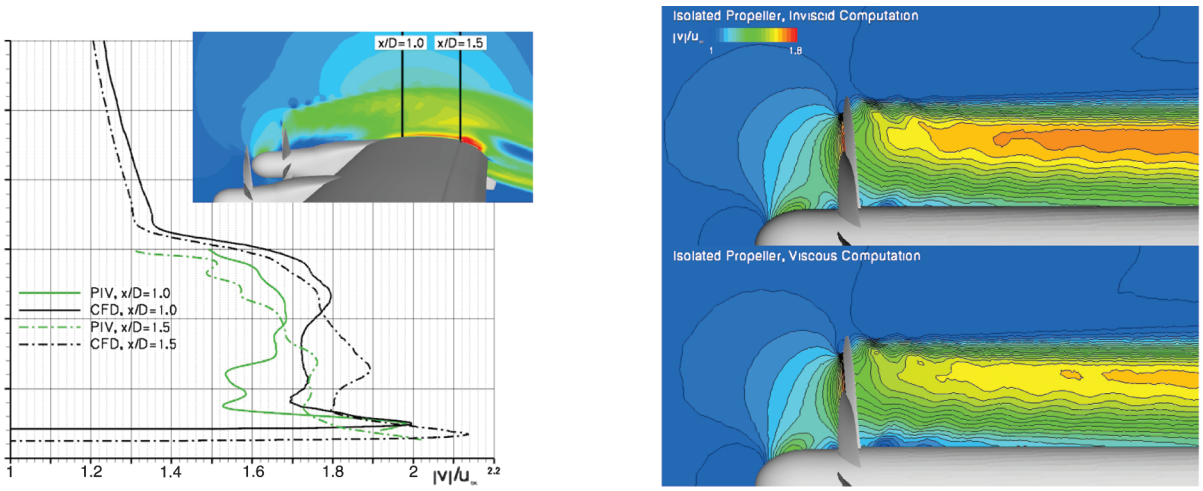

a) Outboard engine centerline absolute velocity profiles at two axial positions

b) Impact of viscous wakes on slipstream development

Fig. 8 Influence of modeling of viscous effects on velocity.

data, the CFD results, in which blade wakes are visible but caused by numerical dissipation, are naturally much weaker and less distinct. This fact is also the root cause for the lower vorticity magnitudes seen in the vortical structures that are seen to move across the wing suction side in Fig. 6. As the inviscid blade modeling does not allow for true viscous wakes to be formed, these vortices cannot be properly represented in the simulation. Thus, improved agreement between the CFD and PIV results can be expected for a full no-slip treatment of all surfaces of the aircraft, including the propeller blades.

V. Suggestions for Further Improvements

The comparison of the uRANS CFD results with the PIV data has shown that the most important deficiency in the simulation was the modeling of the blades as inviscid surfaces. Although this was a necessary simplification at the time, as these simulations were performed to keep the mesh size manageable, the availability of new, large, high-performance cluster computers make a more realistic fully viscous computation feasible. It is expected that such a computation will eliminate the main shortcomings found in the present uRANS results, that is, the increased propeller slipstream velocities and the underprediction in blade wake strength.

The unphysical numerical dissipation inherent to a CFD simulation is, of course, still a primary focus area for future improvements. Further mesh refinement is a straightforward way to sustain the relevant flow features. Along the same lines, perhaps the introduction of structured meshes in the propeller slipstream region, employing the flexibility of the Chimera mesh approach, should be investigated in regard to its potential of reducing numerical dissipation levels while keeping mesh sizes at a reasonable level. Vortical correction models can be used instead of the one-equation Spalart–Allmaras model as modified by Edwards. A step beyond would be the investigation of Reynolds-stress turbulence models, which have achieved a degree of maturity in the recent past that warrants a study of their benefit for the simulation of unsteady propeller flowfields.

The advances made in both the experimental as well as the numerical investigations of propeller flows make the two disciplines a very powerful and complementary tool in the design of propeller–airframe integration, beyond the great benefit of having validation data for CFD simulations. The availability of the full 3-D flowfield data from the numerical simulations is a distinct advantage. As the PIV measurements here deliver only the 2-D vector flowfield in a limited number of planes, the interpretation of the complex flow features is at times difficult. Through a comparison with the CFD data set, a more complete understanding of the aerodynamic interactions is possible. In addition, each approach can serve to support the efficient application of the other. As discussed in detail in the previous sections, the analysis of the experimental data can serve as guidance for the preparation of a numerical analysis in terms of mesh resolution requirements, for example. With the continued deployment of larger and more powerful computer clusters, the running of large-scale unsteady numerical simulations is becoming more and more feasible. Thus, it is possible that, even for these complex simulations, the numerical results can serve to aid in the set up of a subsequent experimental test campaign, for example, highlighting the need for detailed PIV measurements in regions of particular interest.

Stereoscopic PIV (three components of the velocity vector) can already be applied to investigate complex regions of airplane models. But for the investigation of turbulent structures, 3-D and, preferably, time resolved data are required. Using standard PIV in a phase-locked fashion, one obtains quasi-phase-resolved velocity fields. For an investigation of the unsteady effects including the time history, it might be more suitable to apply time-resolved PIV. This could provide a further validation check for the purpose of examining the extent of the unsteady phenomena, as are observed, for example, in the time history of the force coefficients (Fig. 3). Recently, tomographic PIV has been applied [25] to time-resolved turbulent investigations. Apparent advantages, apart from the instantaneous velocity components, are the availability of the full velocity gradient tensor as well as the stress tensor. Such data may be dispensable in an industrial environment, but it is of great importance for gaining or determining confidence in the computational codes. Such experimental data complement CFD analysis and open a whole new branch of validation needs. Synergetic efforts and dedicated validation programs have to be developed that allow one to address the extents of turbulence modeling under realistic conditions. Measurements can be envisaged in which both tomographic PIV, for detailed investigations (junctions, curved sections, transition regions), and stereoscopic PIV, for an overall assessment of the velocity conditions, are performed in parallel.

VI. Conclusions

The experimental and computational analysis on complex curved 3-D shapes for highly periodical and unsteady flows requires special attention. In a combined effort, CFD and PIV have been applied to investigate vortical structures, which dominate propeller flow. Phase-locked PIV and unsteady RANS and have been applied to study the flow phenomena. Although the underlying RANS modeling depends on the velocity decomposition and Reynolds stress distributions, these data are readily available from the PIV measurements. An assessment of velocity and turbulence properties reveals that an overall good agreement between unsteady RANS calculations and phase-locked PIV experiments is achieved for the conditions studied in this paper. Higher velocities in the wake are obtained with CFD

and are caused by the inviscid blade modeling. Similarities in vortex position and wake development are obtained between the PIV and CFD results. Difficult vortex interactions appear at the slipstream edge in the PIV results, due to a (small) random fluctuation of the propeller revolutions during the experiments. There is, however, a big difference between PIV and CFD in the vortex structure organization of the blade wakes and in the wing boundary-layer–slipstream interaction due to strong dissipative terms in the uRANS models. This is further supported by the difference in the circulation distribution in the tip vortices region.

For future investigations, the following considerations may be of relevance. It might be suitable to perform time-resolved PIV measurements for a more detailed understanding of unsteady events. PIV data can be used as boundary condition velocity data or as input velocity data (including a perturbed velocity field) for CFD calculations. Wind-tunnel effects (sting support, etc.) could be modeled in a CFD calculation, which would allow an even better comparison with experimental data. A concurrent advancement of both computations and experiments ultimately leads to an enhanced design optimization process. Recent advancements in both numerical and experimental areas open new doors for future validation and verification possibilities for sophisticated airplane configurations.

Acknowledgments

The authors greatly acknowledge Airbus for providing support during the experiments and allowing the publication of the present data. The measurement campaign was performed as part of a close collaboration with Airbus and was conducted within the Innovative Hochauftriebs-Konfigurationen–New Concepts for High-Lift Configurations German research project.

References

[1] Fujii, K., "Progress and Future Prospects of CFD in Aerospace—Wind Tunnel and Beyond," *Progress in Aerospace Sciences*, Vol. 41, 2005, pp. 455–470. doi:10.1016/j.paerosci.2005.09.001

[2] Stürmer, A., "Unsteady CFD Simulations of Propeller Installation Effects," AIAA Paper 2006-4969, July 2006.

[3] Reckzeh, D., "Aerodynamic Design of the A400M High-Lift System," *26th Congress of the International Council of Aeronautical Sciences*, ICAS Secretariat Paper 2.7.2, Sept. 2008.

[4] Oberkampf, W. L., and Trucano, T. G., "Verification and Validation in Computational Fluid Dynamics," *Progress in Aerospace Sciences*, Vol. 38, 2002, pp. 209–272. doi:10.1016/S0376-0421(02)00005-2

[5] Marvin, J. G., "Accuracy Requirements and Benchmark Experiments for CFD Validation," NASA Rept. TM-100087, 1988.

[6] Schröder, A., Pallek, D., Geisler, R., Lauke, T., Herr, M., Geyr, H. v., and Dierksheide, U., "Particle Image Velocimetry as Validation Tool in Aeronautics," AIAA Paper 2009-1518, Jan. 2009.

[7] Boyle, F. J., Flaherty, M. P. O., and Eaton, J. A., "Comparison of PIV Measurements with CFD Predictions for a High Speed Propeller," AIAA Paper 99-2387, June 1999.

[8] Cho, J., and Cho, J., "Quasi-Steady Aerodynamic Analysis of Propeller-Wing Interaction," *International Journal for Numerical Methods in Fluids*, Vol. 30, 1999, pp. 1027–1042. doi:10.1002/(SICI)1097-0363(19990830)30:8<1027::AID-FLD878>3.0.CO;2-R

[9] Raffel, M., Willert, C. E., Wereley, S. T., and Kompenhans, J., *Particle Image Velocimetry: A Practical Guide*, 2nd ed., Springer–Verlag, Berlin/Heidelberg, 2007, Chap. 2.

[10] Stanislas, M., Kompenhans, J., and Westerweel, J., *Particle Image Velocimetry: Progress Towards Industrial Application*, Kluwer Academic, Dordrecht, The Netherlands, 2000.

[11] Roosenboom, E. W. M., Heider, A., and Schröder, A., "Investigation of the Propeller Slipstream with Particle Image Velocimetry," *Journal of Aircraft*, Vol. 46, 2, 2009, pp. 442–449. doi:10.2514/1.33917

[12] Henne, U., "Application of the PSP Technique in Low Speed Wind Tunnels," *New Results in Numerical and Experimental Fluid Mechanics V,* Notes on Numerical Fluid Mechanics and Multidisciplinary Design, Vol. 92, edited by H.-J. Rath, C. Holze, H.-J. Heinemann, R. Henke, and H. Hönlinger, Springer, New York, 2006, pp. 41–49, ISBN 9783540332862.

[13] Stasicki, B., Ehrenfried, K., Dieterle, L., Ludwikowski, L., and Raffel, M., "Advanced Synchronization Techniques for Complex Flow Field Investigations by Means of PIV," *Proceedings of the 4th International Symposium on PIV,* DLR, Institute of Aerdynamic and Flow Technology Paper 1188, Sept. 2001.

[14] Kähler, C. J., Sammler, B., and Kompenhans, J., "Generation and Control of Tracer Particles for Optical Flow Investigations in Air," *Experiments in Fluids*, Vol. 33, No. 6, Dec. 2002, pp. 736–742.doi: 10.1007/s00348-002-0492-x

[15] Westerweel, J., and Scarano, F., "Universal Outlier Detection for PIV Data," *Experiments in Fluids*, Vol. 39, 2005, pp. 1096–1100. doi:10.1007/s00348-005-0016-6

[16] Gerhold, T., "Overview of the Hybrid RANS Code TAU," *Notes on Numerical Fluid Mechanics and Multidisciplinary Design*, Vol. 89, MEGAFLOW—Numerical Flow Simulation for Aircraft Design, edited by N. Kroll, and J. K. Fassbender, Springer–Verlag, Berlin/Heidelberg, 2005, Chap. 5.

[17] Spalart, P., and Allmaras, S., "A One-Equation Turbulence Model for Aerodynamic Flows," AIAA Paper 92-0439, Jan. 1992.

[18] Edwards, J., and Chandra, S., "Comparison Of Eddy-Viscosity-Transport Turbulence Models for Three-Dimensional, Shock Separated Flows," *AIAA Journal*, Vol. 34, No. 4, 1996, pp. 756–763. doi:10.2514/3.13137

[19] Jameson, A., "Time Dependent Calculations Using Multigrid, with Applications to Unsteady Flows Past Airfoils and Wings," *10th Computational Fluid Dynamics Conference*, 1991.

[20] Madrane, A., Heinrich, R., and Gerhold, T., "Implementation of the Chimera Method in the Unstructured Hybrid DLR Finite Volume TAU-Code," AIAA Paper 91-1596, Oct. 2002.

[21] Madrane, A., Raichle, A., and Stürmer, A., "Parallel Implementation of a Dynamic Overset Unstructured Grid Approach," *European Congress on Computational Methods in Applied Sciences and Engineering* [CD-ROM] 951-39-1868-8 (second edition) and 951-39-1869-6 (second edition), Paper 14, July 2004.

[22] Durand, W. F., *Aerodynamic Theory Volume IV,* Dover, New York, 1963.

[23] Dacles-Mariani, J. S., Rogers, S., Kwak, D., Zillac, G. G., and Chow, J. S., "A Computational Study of Wingtip Vortex Flowfield," AIAA Paper 93-3010, 1993.

[24] Dacles-Mariani, J. S., Kwak, D., and Zillac, G., "Accuracy Assessment of a Wingtip Vortex Flowfield in the Near-Field Region," AIAA Paper 96-0208, 1996.

[25] Schröder, A., Geisler, R., Elsinga, G. E., Scarano, F., and Dierksheide, U., "Investigation of a Turbulent Spot and a Tripped Turbulent Boundary Layer Flow Using Time-Resolved Tomographic PIV," *Experiments in Fluids*, Vol. 44, No. 2, 2008, pp. 305–316. doi:10.1007/s00348-007-0403-2